



New route toward integrating large nickel nanocrystals onto mesoporous carbons

Ying Yang ^{a,*}, Xinsong Li ^a, Feng Yang ^a, Wen Zhang ^a, Xin Zhang ^{a,*}, Yang Ren ^b

^a State Key Laboratory of Heavy Oil Processing, China University of Petroleum, No. 18, Fuxue Road, Changping District, Beijing 102249, China

^b X-ray Science Division, Argonne National Laboratory, 9700 S. Cass Ave., Argonne, IL 60439, USA

ARTICLE INFO

Article history:

Received 9 July 2014

Received in revised form 4 September 2014

Accepted 23 September 2014

Available online 2 October 2014

Keywords:

Nickel nanocrystals

Mesoporous carbon

Soft-templating approach

4-Nitrophenol reduction

Magnetic separation

ABSTRACT

Integrating large and magnetic transition metal nanocrystals onto mesoporous carbons is of great importance owing to their low cost, easy separation and great potential in various applications. Herein we firstly report large nickel nanocrystals (Ni NCs, 30–75 nm) *in situ* integrated onto mesoporous carbons (MC), synthesized via block copolymer-directed self-assembly of nickel acetate and 8-quinolinol modified chitosan under neutral conditions assisted by tetraethyl orthosilicate before pyrolysis and silica removal. This neutral one-pot synthesis not only renders evenly dispersed Ni NCs firmly attached on the mesoporous carbonaceous framework without using any stabilizer, but also creates larger Ni NCs as compared to those prepared by acidic and basic synthetic routes. It is found that all nickel catalysts can be magnetically separated easily; and the Ni NC size, microstructure and the carbonaceous support morphology are well adjusted by variation of the pyrolysis temperature, which in turn affects the catalytic properties of Ni NCs towards 4-nitrophenol reduction. The Ni NC functionalized mesoporous carbon pyrolyzed at 750 °C (Ni-MC-750) simultaneously possessing twinned microstructure and carbon nanotube morphology, exhibits the highest catalytic efficiency. High-energy X-ray diffraction, N₂ adsorption/desorption, transmission electron microscopy, infrared spectroscopy, X-ray absorption fine structure and Raman spectroscopy studies, as well as the comparative catalytic tests have demonstrated these points.

© 2014 Elsevier B.V. All rights reserved.

1. Introduction

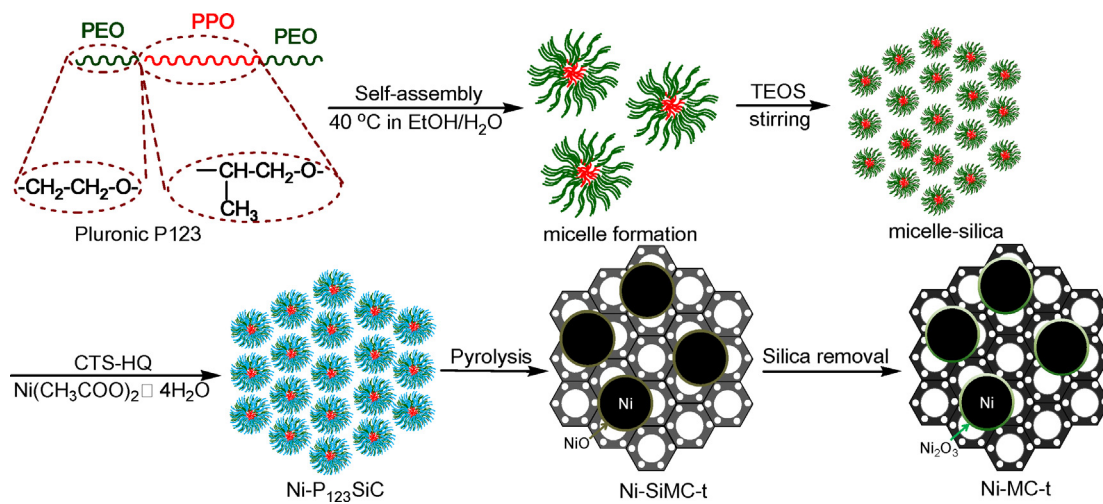
To overcome the problem pertaining to the environmental pollution, green processes have been recently achieved *via* chemical transformations by using green solvents, nontoxic chemicals and ambient reaction conditions. In this aspect, the disposal of nitro compounds is an area of intensive research [1–6]. Nitrophenols are among the most common organic pollutants in industrial and agricultural wastewaters. In particular, 4-nitrophenol (4-NP) is a notorious industrial pollutant exhibiting high solubility and stability in water [7,8]. It is therefore important to develop effective methods for its removal. There are various methods including microbial degradation, catalytic oxidation and electrochemical treatment, have been well developed for its disposal [9–11]. However, the catalytic reduction of 4-NP to 4-aminophenol (4-AP) by using sodium borohydride, which is widely used in sewage

treatment, is considered to be the most efficient, green and economical approach [12–15], and the reduction product namely, 4-AP, has great industrial relevance such as for aniline and paracetamol production [16]. Hence, various catalysts, including precious or doped precious metals [17–21], non-precious metals, mainly Ni-containing nanostructures [17,22–25], and metal-free catalysts [26], have been investigated for this process. Among which, magnetic transition metal nanocrystals (NCs) are much favored since they are low cost, and make the separation process easy by means of an external magnetic field, avoiding the conventional filtration or centrifugation procedures, which is a key obstacle preventing the industrial scale application. In spite of their significant virtues, these magnetic NCs, especially in small size, are prone to agglomeration during usage owing to their high surface energy, which will remarkably lower their catalytic activity and reduce the lifetime. Therefore, creating large NCs and dispersing them on porous supports are vital for construction of economical and persistent nanocatalysts for wastewater treatment.

Magnetic NCs are always immobilized on porous supports, including silica, alumina, titania, zirconia, magnesia and carbon

* Corresponding authors. Tel.: +86 10 89734979; fax: +86 10 89734979.

E-mail addresses: catalyticscience@163.com (Y. Yang), [\(X. Zhang\).](mailto:zhangxin@cup.edu.cn)



Scheme 1. Schematic description of the Ni-MC-t synthesis.

[27–32]. Amongst them, porous carbonaceous supports are the most frequently used, and proved to be superior to oxide carriers, due to their chemical inertness and excellent stability under both acid and basic conditions. So activated carbon, because of its large specific surface area and high pore volume, is widely used as the support. However, the micropore size restricts its further application owing to the difficulty in large molecule transportation [33]. Therefore, mesoporous carbons (MC) with uniform large pores and high surface area are much in demand. Recent advances in the fabrication of NCs onto MC focus on the hard-templating approach to infiltrate an appropriate carbon precursor (e.g. furfuryl alcohol, sucrose) and metal source (Fe, Co and Ni compounds) into the mesopores of the silica template, followed by thermal polymerization, carbonization and subsequent silica dissolution [34–37]. It is demonstrated that SBA-15 coated with 2,3-dihydroxynaphthalene (DHN) and then impregnated with nickel salt and heated, results in mesoporous carbons with evenly dispersed Ni NCs [38]. However, this multi-step synthetic procedure is time-consuming, including repeated impregnation with carbon and/or metal precursors, which may severely hamper the broad application of these composite materials. Recently, in the case of soft-templated carbons, the incorporation of inorganic species to the carbon framework can be done directly during the self-assembly process. So adding the metal salt to the reaction mixture involving the polymerizable precursors and block copolymer templates, can facilitate its transformation into metal NCs embedded in the carbon matrix during thermal treatment. This concept is well demonstrated by Zhao's group; they use nickel nitrate as the metal precursor, resol as the carbon source, and Pluronic F127 as the template in the one-pot synthesis to obtain MCs with evenly distributed Ni NCs (16–20 nm, 10 wt% Ni) [39]. However, more nickel precursor has to be introduced to prepare large Ni NCs, since possible Ni leaching cannot be avoided under the acidic synthetic condition. Our previous studies demonstrate that larger Ni NCs (25–40 nm) can be realized by CTAB-directed self-assembly of modified chitosan and nickel nitrate (10 wt%) under basic conditions [40,41]. Unfortunately, the particle size cannot be further improved even increasing Ni percentage to *ca.* 20 wt%. It is probable that in the presence of ammonia, the formed nickel ammine was dissolved into the reaction mixture, lowering the Ni loading. Therefore, it is speculated that under neutral synthetic conditions, much larger Ni NCs would be prepared since more Ni species could be captured.

We herein firstly report large nickel nanocrystals (Ni NCs, 30–75 nm, *ca.* 20 wt%) *in situ* integrated onto mesoporous carbons

(MC), synthesized via Pluronic P123-directed self-assembly of nickel acetate and 8-quinolinol modified chitosan under neutral conditions assisted by tetraethyl orthosilicate before pyrolysis and silica removal. This silica-assisted strategy strengthens the interaction between chitosan and P123 *via* the polymerization of chitosan with silica, rendering "homogeneous" interpenetrating silica–chitosan frameworks with evenly dispersed nickel complexes inserted, leading to homogeneously distributed Ni NCs on the silica–carbon frameworks in the resulting pyrolyzed samples. Silica removal created more exposed and magnetically recoverable Ni NCs, and their size, microstructure, carbonaceous support morphology, and the corresponding catalytic performances towards 4-nitrophenol reduction can be facilely tuned by variation of the pyrolysis temperature.

2. Experimental

2.1. Materials preparation

Ni NCs were *in situ* integrated onto the MCs *via* construction of P123-directed silica–chitosan–nickel assemblings (Ni-P₁₂₃SiC) before pyrolysis and silica removal. First, 8-quinolinol modified chitosan, CTS-HQ, was facilely synthesized from 5-chloromethyl-8-quinolinol hydrochloride (**1**), involving a two-step chemical transformation from 8-quinolinol (see Supporting Information and Figs. S1–S6). Then, TEOS, CTS-HQ and $\text{Ni}(\text{CH}_3\text{COO})_2 \cdot 4\text{H}_2\text{O}$ were respectively used as silica, carbon and metal precursors, and added stepwise to synthesize P123-directed precursor composite before pyrolysis and silica removal (Scheme 1). The molar ratio of the precursor gel in the preferred preparation is: 1 CTS-HQ:0.5 $\text{Ni}(\text{CH}_3\text{COO})_2 \cdot 4\text{H}_2\text{O}$:0.017 P123:0.55 TEOS:66.5 H_2O :19.6 EtOH. The mixture was stirred at 40°C for 20 h and then transferred into a polypropylene bottle and reacted at 100°C under static conditions for 48 h. The as-made product was washed, dried and pyrolyzed in a tubular furnace under N_2 atmosphere. The heating rate was $2^\circ\text{C}/\text{min}$ below 250°C and $5^\circ\text{C}/\text{min}$ above 250°C , and the pyrolysis was carried out at 550, 750 and 950°C for 2 h, respectively. The resulting solid were denoted as Ni-SiMC-t, and were subjected to alkaline etching with 3.0 M NaOH solution to remove silica layers, affording Ni-MC-t, where *t* represents the carbonization temperature. For comparison, nickel-free mesoporous carbon (MC-750) was synthesized according to the above procedure with the maintenance of the total precursor compounds except for nickel acetate.

2.2. Characterization

N_2 adsorption/desorption isotherms were recorded at 77 K with a Micromeritics Tristar II 3020. Before measurements, the samples were outgassed at 300 °C for 3 h. The specific surface area was calculated by using the Brunauer–Emmett–Teller (BET) method and the pore size distributions were measured by using Barrett–Joyner–Halenda (BJH) analyse from the adsorption branch of the isotherms. Morphology and microstructure were analyzed using a FEI Tecnai G2 F20 TEM equipped with an energy dispersive X-ray spectroscopic analyzer operated at a voltage of 200 kV. Synchrotron X-ray diffraction measurements were performed at the 11-ID-C beamline of the Advanced Photon Source at Argonne National Laboratory. High-energy X-rays of 115 keV energy and 0.6 mm × 0.6 mm beam size were used to obtain two-dimensional (2D) diffraction patterns in the transmission geometry using a PerkinElmer large area detector placed at 1.6 m from the sample. X-ray absorption fine structure (XAFS) was carried out on a beamline at the 20-ID and 20-BM at Advanced Photo Source (APS) at Argonne National Laboratory. The XAFS data were obtained in the transmission mode at the Ni K-edge (8333.0 eV). For the Ni K-edge scan, a Ni foil was placed between the transmission and reference ion chambers. The XAFS data were processed using the Athena software for background removal, post-edge normalization, and XANES analysis. The extended X-ray absorption fine structure (EXAFS) data were analyzed using Artemis software, which implemented FEFF (Supporting Information). Raman spectra were recorded with a HORIBA Jobin Yvon HR800 with a microscope attachment. The laser wavelength of 633 nm was focused using a diffraction limited spot, and the scan time was 2 s for each sample. The infrared spectra of samples were recorded in KBr disks using a NICOLET impact 410 spectrometer. X-ray photoelectron spectroscopy (XPS) was performed on a Thermo ESCALAB 250Xi X-ray photoelectron spectrometer (employing a monochromated Al-K α) X-ray source ($h\nu = 1486.6$ eV). The C 1s line (284.6 eV) was used as the reference to calibrate the binding energies (BE). Magnetic properties were measured by using a vibrating sample magnetometer (PTMS-VSM) with a maximum applied continuous field of 10,000 G at room temperature.

Nickel content was estimated by inductively coupled plasma atomic emission spectroscopy (ICP-AES) analysis conducted on a PerkinElmer emission spectrometer. Each 10 mg sample of vacuum-dried material was placed in a digester with PTFE lined, and dissolved in 3 ml of boiling aqua fortis solution combined with 2 ml of H_2O_2 . Microwave digestion was carried out for 30 min to completely dissolve the metal species. After cooling, each solution was filtered through a 0.45 μ m polyethersulfone filter and then submitted for metal analysis.

2.3. Catalytic reduction of 4-nitrophenol

The reduction of 4-NP was carried out in a quartz cuvette and monitored by using a UV-vis spectroscopy (754PC) at room temperature. For comparison, the yellow aqueous 4-NP solution was prepared and measured prior to monitoring the change of absorption. A total of 25 μ l of aqueous 4-NP solution (0.01 M) was mixed with 2.5 ml of fresh $NaBH_4$ (0.01 M) solution. Subsequently, a given amount of nickel catalyst was added to start the reaction, and the UV spectrometry was employed to monitor the reduction by measuring the absorbance of the solution at 400 nm as a function of time. The solution was *in situ* measured at certain intervals to obtain the successive information about the reaction. After the reaction was finished, the catalyst was quickly separated from the solution using a NdFeB magnet, rinsed with water and re-dispersed into the mixture of new reactants to initiate another reaction cycle.

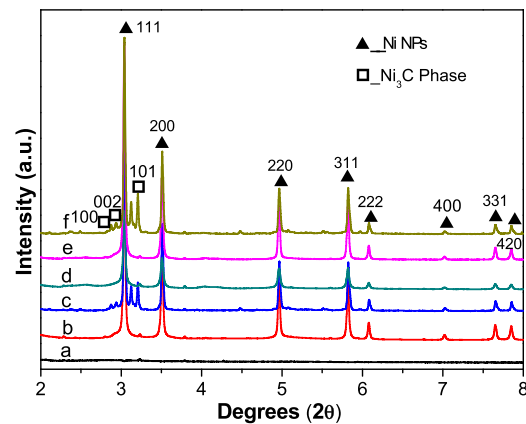


Fig. 1. High-energy X-ray diffraction patterns of (a) Ni-P₁₂₃SiC precursor compound, (b) Ni-SiMC-750, (c) Ni-SiMC-950, (d) Ni-MC-550, (e) Ni-MC-750 and (f) Ni-MC-950.

3. Results and discussion

3.1. Understanding the synthetic strategy

In this study, naturally-occurring macromolecule, chitosan, is chosen as the carbon precursor, and was firstly modified by 5-chloromethyl-8-quinolinol to enhance its chelation with nickel ions, interaction with surfactant P123 via hydrogen bonding, and condensation with silica in neutral aqueous phase, facilitating the formation of P123-directed silica–chitosan–nickel mesophase. This silica–chitosan–nickel mesophase provides an interpenetrating framework with a “reinforced-concrete”-like structure; both “reinforcing-steel-bar” silicate and “concrete” carbons form the mesostructured framework with evenly dispersed Ni complex inserted. Owing to the difference in chemical and thermal stability between chitosan and surfactant P123, the following pyrolysis is a unique “one stone, three birds” strategy to remove P123, carbonize CTS-HQ and reduce nickel ions by the *in situ* formed reducible carbon species, like CO and C, in a single step. The presence of silicates in nanocomposites dramatically inhibits framework shrinkage during the pyrolysis, and removing the silica affords replicated intercrossed carbonaceous mesostructure, during which the Ni NCs are further exposed.

3.2. Sample characterization

High-energy X-ray diffraction examination of Ni-containing samples can detect all diffractions in a short duration. As shown in Fig. 1, the precursor composite Ni-P₁₂₃SiC exhibits no diffractions as expected. Upon pyrolysis, all Ni-SiMC-*t* and Ni-MC-*t* samples display characteristic of fcc-structured Ni (JCPDS file 04-0805) at (111), (200), (220), (311) and (222) diffractions, indicating the formation of Ni NCs [42]. However, the diffraction intensity varies with the pyrolysis temperature. Samples pyrolyzed at 950 °C renders additional characteristic (100), (002) and (101) diffractions owing to rhombohedric-centered Ni₃C phase [43], originating from the thermal reaction of nickel species with graphitic carbon at high temperature [44]. The small angle X-ray scattering pattern for both Ni-SiMC-750 and Ni-MC-750 shows three weak peaks at q values of 0.212, 0.324 and 0.440 with a ratio of 1:3^{1/2}:2 (Figs. S7,8), associating with 10, 11 and 20 reflections of low 2D hexagonal symmetry with $p6m$ space group [45].

TEM images clearly show numerous spherical NCs homogeneously dispersed on the carbonaceous frameworks of Ni-MC-550, Ni-MC-750 and Ni-MC-950, and display a narrow particle size distribution with an increasing average diameter from 35.7 to 71.0 nm

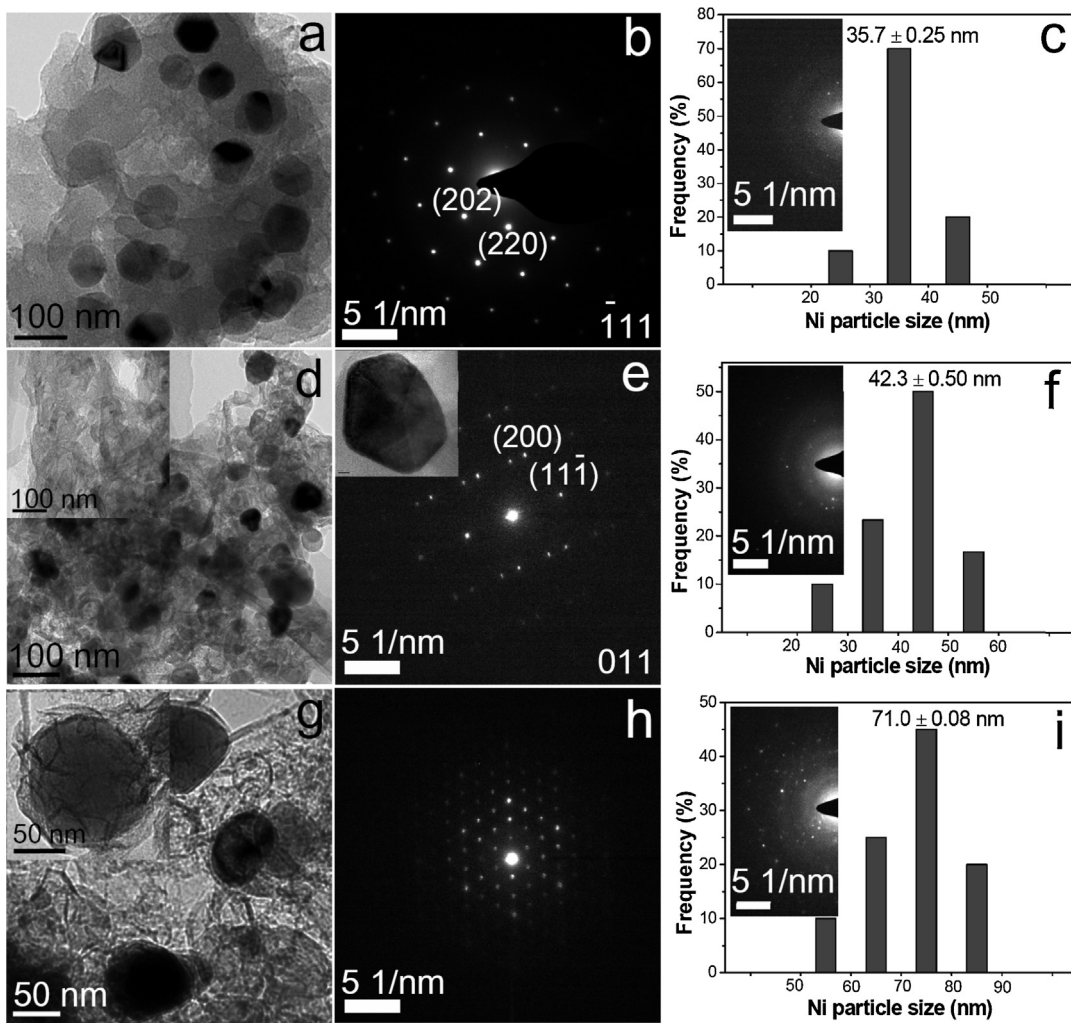


Fig. 2. TEM images, micro electron diffractions of single particle, and the particle size distributions (selected area electron diffractions, inset) for (a–c) Ni–MC–550, (d–f) Ni–MC–750 and (g–i) Ni–MC–950.

(Fig. 2), indicating the easy aggregation and growing to large particles at higher temperature. Electron microdiffraction of single Ni NC demonstrates the *fm-3m* symmetrical structure (Fig. 2b,e,h); the Ni NCs in Ni–MC–550 and Ni–MC–950 are monocrystalline, while they are twinned in Ni–MC–750 [46]. Selected area electron diffraction (SAED) patterns for Ni–MC–t samples demonstrate the diffraction spots and diffraction rings assigned to crystalline Ni NCs and graphitic carbons [47], respectively. On the other hand, the morphology of carbonaceous supports changes from lapped nanoflakes, carbon nanotubes to carbon fibers when the carbonization temperature is elevated from 550, 750 to 950 °C, respectively, suggesting the different growth pathways.

FT-IR spectra are sensitive to the change occurred at different synthetic steps. As illustrated in Fig. 3, the precursor composite Ni–P₁₂₃SiC shows C–H stretches at 2962 and 2927 cm^{−1} ascribed to PPO and PEO moieties from the surfactant P123, and the characteristic phenyl and pyridyl vibrations between 1760 and 1300 cm^{−1}, as well as the silica framework vibration modes at 1098 and 465 cm^{−1} [48–50], confirming that CTS–HQ and silica have been incorporated into P123-directed silica–chitosan–nickel assemblings (Fig. 3a). However, only the characteristic silica peaks remain upon pyrolysis, indicating that P123 removal and CTS–HQ carbonization occurred (Fig. 3b). Further silica removal is supported by the disappearance of silica peaks after alkaline etching (Fig. 3c–e).

The X-ray absorption fine structure (XAFS) reveals the transition and local structure of Ni-containing species. As shown in Fig. 4, compared to Ni–P₁₂₃SiC, all pyrolyzed samples show the decreased white line intensity along with the newly present pre-edge peak at ca. 8335 eV, suggesting the Ni(II) species are mostly reduced

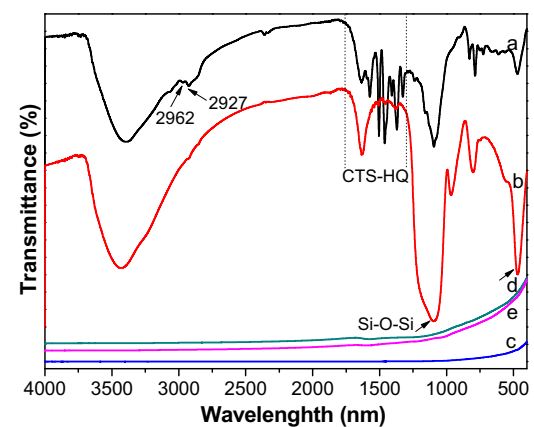


Fig. 3. FT-IR patterns of (a) Ni–P₁₂₃SiC, (b) Ni–SiMC–750, (c) Ni–MC–550, (d) Ni–MC–750 and (e) Ni–MC–950.

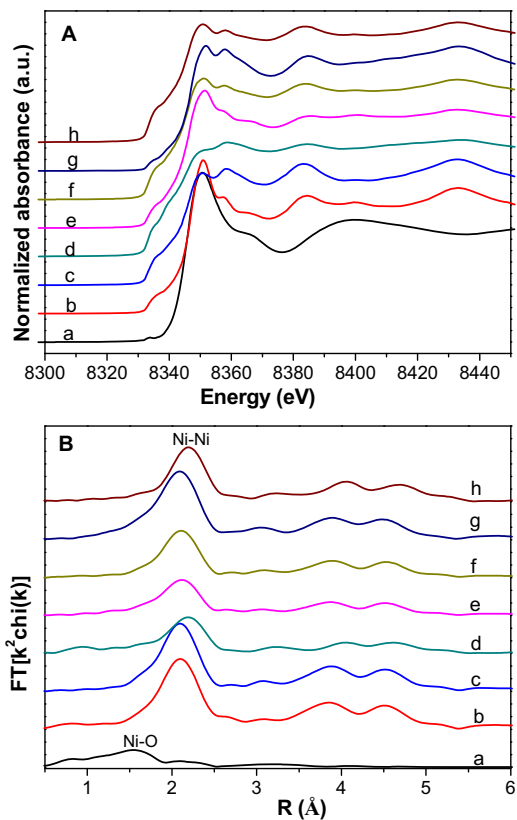


Fig. 4. (A) Ni K-edge XANES and (B) the corresponding Fourier transformed EXAFS spectra for (a) Ni-P₁₂₃SiC, (b) Ni-SiMC-550, (c) Ni-SiMC-750, (d) Ni-SiMC-950, (e) Ni-MC-550, (f) Ni-MC-750, (g) Ni-MC-950 and (h) Ni foil.

[51,52]. In the corresponding k space, stronger oscillations at a higher k region of $k > 8 \text{ \AA}^{-1}$ was observed over pyrolyzed samples (Fig. S9), indicating the dominance of high Z backscatters, which would be Ni in our system. Correspondingly, the Fourier transformed EXAFS data (r space) exhibit one prominent peak at ca. 2.2 \AA from the Ni-Ni contributions for Ni-SiMC- t and Ni-MC- t series, different from the dominated Ni-N pairs at ca. 1.6 \AA for Ni-P₁₂₃SiC. On the other hand, the Ni-Ni peak intensity, proportional to the coordination number, varies with the pyrolysis temperature and the presence of silica or not. To eliminate the systemic error, wider range ($1.6\text{--}5.9 \text{ \AA}$) of fitting was carried out (Fig. S10), and the fitting result was shown in Table 1. For Ni-SiMC- t series, the Ni-Ni coordination number decreases from 14.1 to 5.4 as the carbonization temperature elevated from 550 to 950 °C, whereas Ni-MC- t series exhibit an increase from 6.4 to 14.4. It is interesting that silica removal brings about a decrease in coordination numbers for samples pyrolyzed at 550 and 750 °C, while an increase for samples

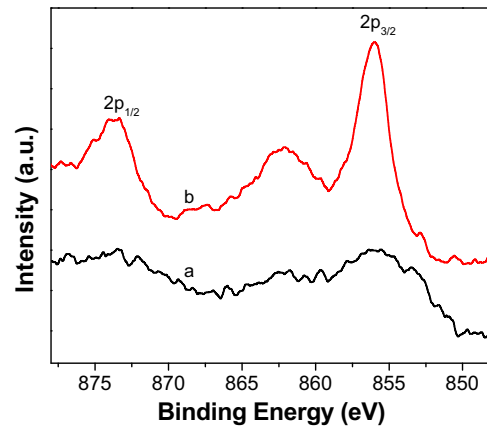


Fig. 5. XPS of Ni_{2p} spectra for (a) Ni-SiMC-750 and (b) Ni-MC-750.

pyrolyzed at 950 °C. The larger coordination number than 12 may be related to the fitting error within ±20%. To investigate the surface properties of Ni NCs, the N1s binding energies were investigated, and the corresponding spectra were shown in Fig. 5. The Ni 2p_{3/2} XPS peak at 855.4 eV coincides with the finding for nickel oxide in Ni-SiMC-750 [53]. The CTS-HQ provides the oxygen source for the oxidation layer formation under the inert atmosphere. However, the feature extending from 855.4 to 856.0 eV is attributed to the formation of nickel trioxide [54], suggesting more oxygen inserted during alkaline washing.

N₂ adsorption reveals that all pyrolyzed samples exhibit an IV type isotherm with an H₄-type hysteresis loop (Fig. 6A), characteristic of mesoporous materials bearing slit pores [55,56], with a narrow pore size distribution centered at ca. 4.3 nm (Fig. 6B). It is observed that the textual parameter varies with the carbonization temperature for both Ni-SiMC- t and Ni-MC- t series. As shown in Table 2, the BET surface areas decrease from $375 \text{ m}^2 \text{ g}^{-1}$ for Ni-SiMC-550 to $174 \text{ m}^2 \text{ g}^{-1}$ for Ni-SiMC-950, and from $317 \text{ m}^2 \text{ g}^{-1}$ for Ni-MC-550 to $179 \text{ m}^2 \text{ g}^{-1}$ for Ni-MC-950, respectively. More chips and larger particles produced during the framework collapse at higher temperature should be responsible for such a decrease. Different from the significantly increased surface areas and pore volumes created upon silica removal reported by Hu et al. [57], Ni-MC-550 and Ni-MC-750 exhibit a decline after alkaline etching, suggesting the further collapse of carbonaceous framework occurred. The local structure of carbonaceous support was investigated by Raman spectroscopy. As shown in Fig. 7, Ni-MC- t samples exhibit D and G bands centered at around 1330 and 1600 cm^{-1} , respectively, arising from the disordered carbon and ordered graphitic sheet [58]. However, the I_G/I_D (relative ratio of G band to D band) value decreases from 0.78 to 0.69 when the carbonization temperature was elevated from 550 to 750 °C.

Table 1

Best fit parameters obtained from the analysis of the Ni K-edge EXAFS spectra.

Materials	First shell	CN ^a	R (Å) ^b	$\sigma^2 (\times 10^{-3}) (\text{\AA}^2)$ ^c	ΔE_0 (eV) ^d	R-factor
Ni-SiMC-550	Ni-Ni	14.1 ± 1.2	2.48 ± 0.003	8.66 ± 0.52	-10.701 ± 0.863	0.010
Ni-SiMC-750	Ni-Ni	13.2 ± 0.7	2.48 ± 0.003	7.48 ± 0.39	-9.291 ± 0.660	0.005
Ni-SiMC-950	Ni-Ni	5.4 ± 1.5	2.48 ± 0.004	5.69 ± 0.69	4.847 ± 0.821	0.020
Ni-MC-550	Ni-Ni	6.4 ± 0.6	2.48 ± 0.003	6.89 ± 0.69	-10.113 ± 1.098	0.020
Ni-MC-750	Ni-Ni	8.0 ± 0.4	2.49 ± 0.003	6.49 ± 0.42	-8.444 ± 0.665	0.008
Ni-MC-950	Ni-Ni	14.4 ± 1.0	2.48 ± 0.008	8.12 ± 0.50	-11.371 ± 0.771	0.010
Ni foil	Ni-Ni	12.0	2.48			

^a CN = coordination number.

^b R = coordination distance.

^c σ^2 = Debye-Waller factor.

^d ΔE_0 = inner potential correction.

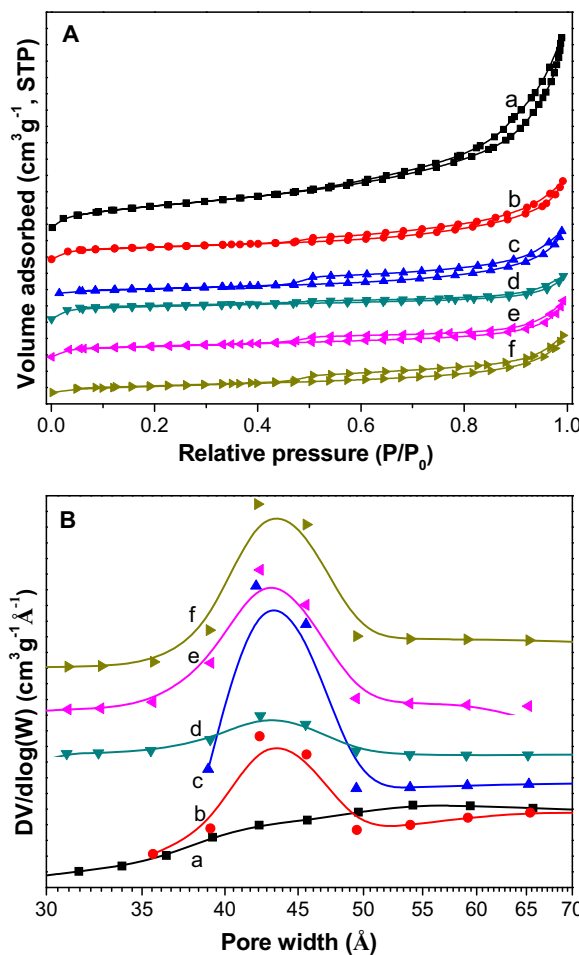


Fig. 6. (A) N₂ adsorption/desorption isotherms and (B) BJH pore size distributions of (a) Ni-SiMC-550, (b) Ni-SiMC-750, (c) Ni-SiMC-950, (d) Ni-MC-550, (e) Ni-MC-750 and (f) Ni-MC-950.

Magnetization curves of the nickel catalysts (Fig. 8) exhibit near-zero coercivities and remanences, suggesting a superparamagnetic nature. The corresponding saturation magnetization strength is 7.9 and 9.0 emu g⁻¹ for Ni-SiMC-750 and Ni-MC-750, respectively, increasing with the etching of silica layer. The values are much lower than that of the bulk Ni (51.3 emu g⁻¹) [59], mainly due to the nanosize effect and the presence of carbon. The magnetic separability of such magnetic composites was tested in an aqueous solution by placing a magnet near the glass bottle. The powder samples can be easily attracted by the magnet and separated from the solution (Fig. 8, inset), suggesting an easy separation process.

Table 2
Textural properties, kinetic constants and turnover frequencies of various catalysts.

Materials	S _{BET} ^a (m ² g ⁻¹)	S _{micro} ^b (m ² g ⁻¹)	V _p (cm ³ g ⁻¹)	V _{micro} (cm ³ g ⁻¹)	D _p ^c (nm)	k × 10 ³ (s ⁻¹)	K (s ⁻¹ g ⁻¹)	Ni loading ^d (wt%)	TOF ^e × 10 ³ (s ⁻¹)
Ni-SMC-550	375	89	0.75	—	5.4	0.02	0.01	11.0	0.0009
Ni-SMC-750	264	153	0.37	0.06	4.3	0.57	0.64	16.8	0.0543
Ni-SMC-950	174	91	0.29	0.03	4.3	1.12	0.66	22.7	0.0314
Ni-MC-550	317	228	0.27	0.10	4.3	0.23	0.23	16.2	0.0200
Ni-MC-750	248	165	0.27	0.07	4.3	1.45	2.76	21.9	0.1100
Ni-MC-950	179	102	0.26	0.04	4.3	0.52	0.43	22.5	0.0160

^a The BET surface areas are obtained from the adsorption branches in the relative pressure range of 0.05–0.20.

^b Microporous volumes are calculated by t-plot method.

^c The pore size distributions are calculated from the adsorption branches by the Barret–Joyner–Halenda (BJH) method.

^d Estimated by ICP-AES.

^e TOF, s⁻¹: (turnover frequency) moles of 4-NP converted per mole Ni per second.

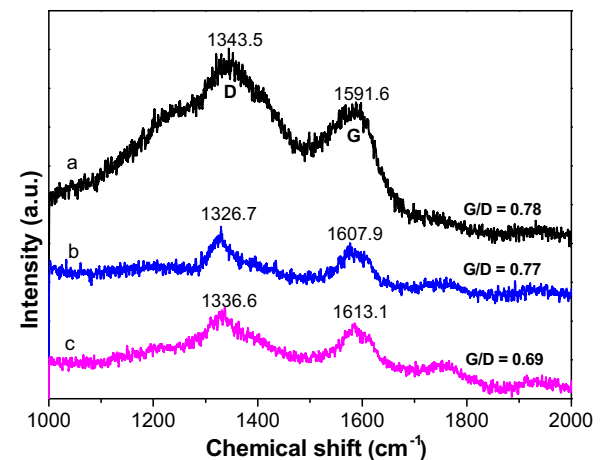


Fig. 7. Raman spectra of (a) Ni-MC-550, (b) Ni-MC-750 and (c) Ni-MC-950.

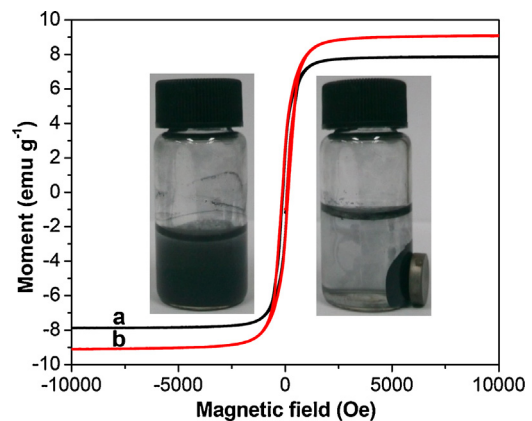


Fig. 8. Magnetization curves of (a) Ni-SiMC-750 and (b) Ni-MC-750, and the optical photo (inset) of Ni-MC-750 in an aqueous solution separated by a magnet.

3.3. Catalytic properties

The catalytic performance towards 4-NP reduction is screened in the presence of NaBH₄. It is well-known that 4-NP solution exhibits a strong absorption peak at 317 nm (Fig. 9A), which is remarkably red-shifted to 400 nm on addition of NaBH₄ due to the nitrophenolate ion formation (*pK_a* = 7.15) [19]. The catalytic reduction of 4-NP can be easily monitored by the reactant 4-nitrophenolate anion ($\lambda_{\text{max}} = 400$ nm) through UV-vis spectrophotometry. A significant decrease in the absorbance at 400 nm associated with the concomitant evolution of a peak at 295 nm (Fig. 9B) indicates the reduction of 4-NP to 4-aminophenol (4-AP).

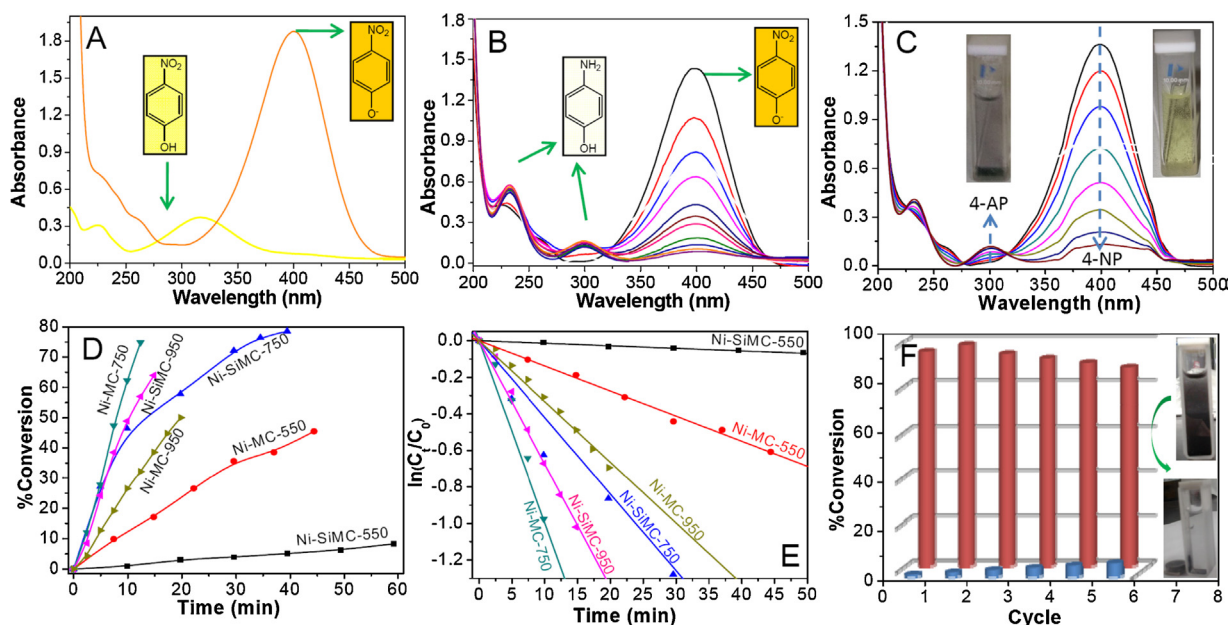
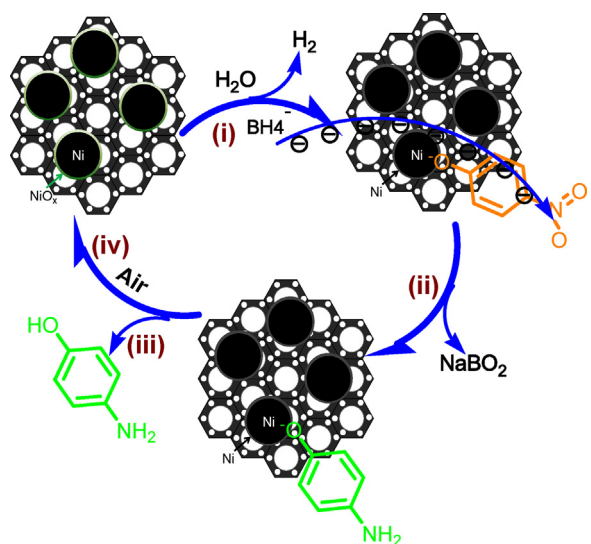


Fig. 9. (A) UV-vis spectra of 4-nitrophenol before and after adding NaBH_4 solution, (B) The reduction of 4-nitrophenol in aqueous solution recorded every 4.93 min over 1.0 mg Ni-SiMC-750, (C) The reduction of 4-nitrophenol in aqueous solution recorded every 2.47 min over 0.6 mg Ni-MC-750, (D) Time dependent conversion of 4-NP reduction catalyzed by various catalysts. (E) The relationship between $\ln(C_t/C_0)$ and reaction time (t) and (F) Catalytic conversion of 4-NP by using recycled Ni-MC-750 at different cycle times.

The catalytic efficiency of pure mesoporous carbon and Ni NC integrated mesoporous carbons towards 4-NP reduction is comparatively studied. The 4-NP conversion is calculated from C_t/C_0 , measured from the relative intensity of absorbance (A_t/A_0) at 400 nm, where C_0 and C_t are the 4-NP concentration at time t and 0, respectively. Fig. 9B and C and Figs. S11–S15 illustrates the absorbance vs reaction time plots towards 4-NP reduction using various catalysts. In presence of MC-750, the adsorption peak at 400 nm remained unaltered even for a couple of days. The reduction proceeds rapidly over Ni catalysts except for Ni-SiMC-550. Fig. 9D describes the relationship between 4-NP conversion and reaction time over different catalysts. It is clear that the reactivity follows the sequence: Ni-MC-750 > Ni-SiMC-950 > Ni-SiMC-750 > Ni-MC-950 > Ni-MC-550 > Ni-SiMC-550. To qualify the reactivity, the reaction is considered as a *pseudo-first-order* reaction with regard to 4-NP only to evaluate the catalytic rate, since the concentration of NaBH_4 largely exceeds that of 4-NP ($C_{\text{NaBH}_4}/C_{\text{4-NP}} = 100:1$). Fig. 9E shows the liner relationship between $\ln(C_t/C_0)$ and reaction time, t , which matches the first-order reaction kinetics well, and the rate constant can be calculated from the rate equation $-\ln(C_t/C_0) = kt$. To compare different catalysts, we calculated the ratio of rate constant K over total weight of nickel catalyst, where $K = k/m$. As shown in Table 2, K values increase over Ni-SiMC- t samples when elevating pyrolysis temperature from 550 to 950 °C, linking to the more coordinatively unsaturated sites; and Ni-MC-750 shows the largest K value of any Ni-MC- t catalyst. On the other hand, silica removal creates more active Ni-MC-550 and Ni-MC-750 than their corresponding parent material; while less active Ni-MC-950 as compared to Ni-SiMC-950. This change rule closely relates to the change of Ni-Ni coordination number. It is clear that Ni-MC-750 shows the largest activity factor (in agreement with the comparison of TOF values listed in Table 2), which is about 2.9 times larger than the previously reported ratio for NiCo_2 alloys ($0.95 \text{ s}^{-1} \text{ g}^{-1}$) [22], and comparative to that for reported Ni NPs in a spherical polyelectrolyte brush nanoreactor ($2.4 \text{ s}^{-1} \text{ g}^{-1}$) [17]. The largest rate constant and TOF value suggest the highest catalytic efficiency of Ni-MC-750 with defected Ni NCs anchored on carbon nanotubes with more coordinatively

unsaturated sites. The best performance also can be ascribed to the rapid electron transfer rate (from BH_4^- ion to 4-NP) through graphitic carbonaceous framework [60,61], and this heterogeneous charge transfer is faster than diffusion. For this reaction, the mechanism of surface reaction was provided by Zhang et al. [62] by investigating the catalytic activity of Ag clusters supported on TiO_2 . They suggested that surface hydrogen is first transferred to the Ag nanoparticles by the decomposition of borohydride. This species then reacts with 4-NP to yield the product 4-AP. The kinetics of the reaction is modeled in terms of a Langmuir–Hinshelwood mechanism, where both reactants need to be adsorbed on the surface prior to reaction [63]. Considering the oxidation layer of nickel oxide coated on the surface of Ni NCs in this study, the proposed mechanism for the 4-NP reduction is described in Scheme 2. (i) The



Scheme 2. Mechanistic model of Langmuir–Hinshelwood mechanism for the reduction of 4-NP to 4-AP by NaBH_4 in presence of Ni NCs.

external nickel (tri)oxide layer was reduced by NaBH₄ rapidly to give Ni(0) species upon mixing. (ii) Because of the chemical interaction between the particle surface and the substrates, the phenolate ions get adsorbed onto the Ni NC surface when present in the aqueous medium, forming the surface complex; Meanwhile, the strong nucleophile NaBH₄, because of its diffusive nature and high electron injection capability, transfers electrons to the substrate via metal particles or carbonaceous support. This helps to overcome the kinetic barrier of the reaction. (iii) Reduction of the 4-NP by *in situ* produced H₂ to form the adsorbed product, 4-AP, and (iv) finally desorption of the product, and the surface Ni(0) species was re-oxidized by ambient air to nickel (tri)oxide when NaBH₄ was fully digested. The rate-determining step is governed by the reaction of the adsorbed species. The adsorption/desorption equilibrium is assumed to be much faster and is modeled in terms of a Langmuir isotherm.

To investigate the reusability, the Ni-MC-750 catalyst was facilely separated using a magnet from the catalytic reaction solution. The catalyst exhibits similar catalytic performance without visible reduction in the conversion for the same reaction time (20 min) even after running for six cycles (Fig. 9F). To further verify its stability, the Ni concentration in the reaction solution was checked by ICP-AES to be less than 0.3 ppm, indicating the negligible leaching of Ni into the liquid phase. Our TEM measurement also shows that the Ni NCs are well retained and there is no coagulation after plenty of repeating catalytic processes (Fig. S16), further suggesting the excellent stability and long life.

4. Conclusion

In summary, large magnetic Ni NCs (30–75 nm) have been *in situ* integrated onto mesoporous carbons *via* construction of P123-directed silica–chitosan–nickel assemblings before pyrolysis and silica removal. The soft-templated large Ni NCs were firstly realized under neutral reaction conditions, and their even dispersion on mesoporous carbons was guaranteed by controlling the metal precursor distribution in the precursor compounds. The variation of pyrolysis temperature tuned the particle size, microstructure, and the carbonaceous support morphology, as well as the catalytic performance towards 4-NP reduction. It is demonstrated that elaborately fabricated Ni-MC-750 shows the best catalytic activity and high stability, ascribing to the combined effect of defected Ni NCs and nanotube morphology of carbonaceous framework. This work reveals new possibilities for designing and fabricating easy separated wastewater treatment catalysts by creating large metal size.

Acknowledgements

Financial support for this research work from the National Natural Science Foundation of China (21303229, 21173269, 91127040 and 51101170), and the Science Foundation of China University of Petroleum, Beijing (2462013YJRC018) is acknowledged. PNC/XSD facilities at the Advanced Photon Source, and research at these facilities, are supported by the US Department of Energy-Basic Energy Sciences, a Major Resources Support grant from NSERC, the University of Washington, the Canadian Light Source and the Advanced Photon Source. Use of the Advanced Photon Source, an Office of Science User Facility operated for the U.S. Department of Energy (DOE) Office of Science by Argonne National Laboratory, was supported by the U.S. DOE under Contract No. DE-AC02-06CH11357. We thank Dr. C. J. Sun for his kind support on EXAFS measurements at Sector 20.

Appendix A. Supplementary data

Supplementary data associated with this article can be found, in the online version, at <http://dx.doi.org/10.1016/j.apcatb.2014.09.056>.

References

- [1] J.M. Zhang, G.Z. Chen, M. Chaker, F. Rosei, D.L. Ma, *Appl. Catal. B: Environ.* 132 (2013) 107–115.
- [2] F. Cardenas-Lizana, D. Lamey, N. Perret, S. Gomez-Quero, L. Kiwi-Minsker, M.A. Keane, *Catal. Commun.* 21 (2012) 46–51.
- [3] Z.Y. Zhang, C.L. Shao, P. Zou, P. Zhang, M.Y. Zhang, J.B. Mu, Z.C. Guo, X.H. Li, C.H. Wang, Y.C. Liu, *Chem. Commun.* 47 (2011) 3906–3908.
- [4] M. Zarejoushghani, M. Moeder, H. Borsdorf, *Anal. Chim. Acta* 798 (2013) 48–55.
- [5] X. Li, X. Wang, S. Song, D. Liu, H. Zhang, *Chem. Eur. J.* 18 (2012) 7601–7607.
- [6] F. Coccia, L. Tonucci, D. Bosco, M. Bressan, N. d'Alessandro, *Green Chem.* 14 (2012) 1073–1078.
- [7] Y.C. Chang, D.H. Chen, *J. Hazard. Mater.* 165 (2009) 664–669.
- [8] J.-R. Chiou, B.-H. Lai, K.-C. Hsu, D.-H. Chen, *J. Hazard. Mater.* 248 (2013) 394–400.
- [9] M.A. Oturan, J. Peiroten, P. Chartrin, A.J. Acher, *Environ. Sci. Technol.* 34 (2000) 3474–3479.
- [10] O.A. O'Connor, L.Y. Young, *Environ. Toxicol. Chem.* 8 (1989) 853–862.
- [11] M.S. Dieckmann, K.A. Gray, *Water Res.* 30 (1996) 1169–1183.
- [12] Y.F. Shen, X.Y. Liu, T.H. Sun, J.P. Jia, *RSC Adv.* 2 (2012) 8867–8882.
- [13] M. Muniz-Miranda, *Appl. Catal. B: Environ.* 146 (2014) 147–150.
- [14] M.M. Mohamed, M.S. Al-Sharif, *Appl. Catal. B: Environ.* 142–143 (2013) 432–441.
- [15] Y. Yang, Y. Guo, F. Liu, X. Yuan, Y. Guo, S. Zhang, W. Guo, M. Huo, *Appl. Catal. B: Environ.* 142–143 (2013) 828–837.
- [16] S. Gazi, R. Ananthakrishnan, *Appl. Catal. B: Environ.* 105 (2011) 317–325.
- [17] Z.M. Zhu, X.H. Guo, S. Wu, R. Zhang, J. Wang, L. Li, *Ind. Eng. Chem. Res.* 50 (2011) 13848–13853.
- [18] X. Huang, X.P. Liao, B. Shi, *Green Chem.* 13 (2011) 2801–2805.
- [19] Y.Y. Lin, Y. Qiao, Y.J. Wang, Y. Yan, J.B. Huang, *J. Mater. Chem.* 22 (2012) 18314–18320.
- [20] G.H. Chang, Y.L. Luo, W.B. Lu, X.Y. Qin, A.M. Asiri, A.O. Al-Youibibc, X.P. Sun, *Catal. Sci. Technol.* 2 (2012) 800–806.
- [21] Z.D. Pozun, S.E. Rodenbusch, E. Keller, K. Tran, W.J. Tang, K.J. Stevenson, G. Henkelman, *J. Phys. Chem. C* 117 (2013) 7598–7604.
- [22] K.-L. Wu, X.-W. Wei, X.-M. Zhou, D.-H. Wu, X.-W. Liu, Y. Ye, Q. Wang, *J. Phys. Chem. C* 115 (2011) 16268–16274.
- [23] P. Sarmah, P. Deka, P. Bharali, *Bull. Catal. Soc. India* 12 (2013) 54–59.
- [24] Z.F. Jiang, J.M. Xie, D.L. Jiang, J.J. Jing, H.R. Qin, *CrystEngComm* 14 (2012) 4601–4611.
- [25] I.H.A.E.I Maksod, E.Z. Hegazy, S.H. Kenawy, T.S. Saleh, *Appl. Surf. Sci.* 255 (2008) 3471–3479.
- [26] X.-K. Kong, Z.-Y. Sun, M. Chen, C.-L. Chen, Q.-W. Chen, *Energy Environ. Sci.* 6 (2013) 3260–3266.
- [27] X.C. Wang, L.Q. Meng, F. Wu, Y.J. Jiang, L. Wang, X.D. Mu, *Green Chem.* 14 (2012) 758–765.
- [28] J.F. Pang, A.Q. Wang, M.Y. Zheng, Y.H. Zhang, Y.Q. Huang, X.W. Chen, T. Zhang, *Green Chem.* 14 (2012) 614–617.
- [29] S. Schimpf, C. Louis, P. Claus, *Appl. Catal. A: Gen.* 318 (2007) 45–53.
- [30] A. Shrotri, A. Kanksale, J.N. Beltramini, H. Gurav, S.V. Chilukuri, *Catal. Sci. Technol.* 2 (2012) 1852–1858.
- [31] E. van Ryneveld, A.S. Mohamed, P.S. van Heerden, M.J. Green, H.B. Friedrich, *Green Chem.* 13 (2011) 1819–1827.
- [32] M. Banu, S. Sivasanker, T.M. Sankaranarayanan, P. Venuvanalingam, *Catal. Commun.* 12 (2011) 673–677.
- [33] J. Lee, J. Kim, T. Hyeon, *Adv. Mater.* 18 (2006) 2073–2094.
- [34] A.-H. Lu, W.-C. Li, A. Kiefer, W. Schmidt, E. Bill, G. Fink, F. Schüth, *J. Am. Chem. Soc.* 126 (2004) 8616–8617.
- [35] A.-H. Lu, W. Schmidt, N. Matoussevitch, H. Bönnemann, B. Spliethoff, B. Tesche, E. Bill, W. Kiefer, F. Schüth, *Angew. Chem. Int. Ed.* 43 (2004) 4303–4306.
- [36] S.M. Holmes, P. Foran, E.P.L. Roberts, J.M. Newton, *Chem. Commun.* 14 (2005) 1912–1913.
- [37] I.S. Park, M. Choi, T.W. Kim, R. Ryoo, *J. Mater. Chem.* 16 (2006) 3409–3416.
- [38] P.F. Fulvio, C. Liang, S. Dai, M. Jaroniec, *Eur. J. Inorg. Chem.* 2009 (2009) 605–612.
- [39] Y.P. Zhai, Y.Q. Dou, X.X. Liu, S.S. Park, C.-S. Ha, D.Y. Zhao, *Carbon* 49 (2011) 545–555.
- [40] Y. Yang, Y. Ren, C.J. Sun, S.J. Hao, *Green Chem.* 16 (2014) 2273–2280.
- [41] Y. Yang, G. Gao, X. Zhang, F.W. Li, *ACS Catal.* 4 (2014) 1419–1425.
- [42] G.Z. Chen, S. Desinan, R. Nechache, R. Rosei, F. Rosei, D.L. Ma, *Chem. Commun.* 47 (2011) 6308–6310.
- [43] V.K. Portnoi, A.V. Leonov, S.N. Mudretsova, S.A. Fedotov, *Phys. Metals Metallogr.* 109 (2010) 153–161.
- [44] C.-P. Luo, S.-X. Qi, N. Li, Z.-D. Lin, *Acta Phys. Sin.* 39 (1990) 1435–1440.
- [45] Y.R. Liu, *J. Mater. Sci.* 44 (2009) 3600–3607.
- [46] G.Z. Chen, S. Desinan, R. Rosei, F. Rosei, D.L. Ma, *Chem. Eur. J.* 18 (2012) 7925–7930.
- [47] Z.X. Wu, Y.Y. Lv, Y.Y. Xia, P.A. Webley, D.Y. Zhao, *J. Am. Chem. Soc.* 134 (2012) 2236–2245.

- [48] X.G. Wang, K.S.K. Lin, J.C.C. Chan, S. Cheng, *J. Phys. Chem. B* 109 (2005) 1763–1769.
- [49] M.R. Maurya, S. Sikarwar, *J. Mol. Catal. A: Chem.* 263 (2007) 175–185.
- [50] M.R. Maurya, A.K. Chandrakar, S. Chand, *J. Mol. Catal. A: Chem.* 270 (2007) 225–235.
- [51] L.S. Sarma, C.-H. Chen, S.M.S. Kumar, G.-R. Wang, S.-C. Yen, D.-G. Liu, H.-S. Sheu, K.-L. Yu, M.-T. Tang, J.-F. Lee, C. Bock, K.-H. Chen, B.-J. Hwang, *Langmuir* 23 (2007) 5802–5809.
- [52] O.M. Daniel, A. DeLaRiva, E.L. Kunkes, A.K. Datye, J.A. Dumesic, R.J. Davis, *ChemCatChem* 2 (2010) 1107–1114.
- [53] M. Salavati-Niasari, F. Mohandes, F. Davar, M. Mazaheri, M. Monemzadeh, N. Yavarinia, *Inorg. Chim. Acta* 362 (2009) 3691–3697.
- [54] Z.Y. Hou, O. Yokota, T. Tanaka, T. Yashima, *Appl. Catal. A: Gen.* 253 (2003) 381–387.
- [55] A. Corma, *Chem. Rev.* 97 (1997) 2373–2419.
- [56] P.A. Robles-Dutenhefner, K.A.D. Rocha, E.M.B. Sousa, E.V. Gusevskaya, *J. Catal.* 265 (2009) 72–79.
- [57] Q.Y. Hu, R. Kou, J.B. Pang, T.L. Ward, M. Cai, Z.Z. Yang, Y.F. Lu, J. Tang, *Chem. Commun.* 6 (2007) 601–603.
- [58] W. Chaikittisilp, M. Hu, H.J. Wang, H.-S. Huang, T. Fujita, K.C.-W. Wu, L.-C. Chen, Y. Yamauchi, K. Ariga, *Chem. Commun.* 48 (2012) 7259–7261.
- [59] P.Z. Si, Z.D. Zhang, D.Y. Geng, C.Y. You, X.G. Zhao, W.S. Zhang, *Carbon* 41 (2003) 247–251.
- [60] X.L. Pan, X.H. Bao, *Acc. Chem. Res.* 44 (2011) 553–562.
- [61] H. Wu, X. Huang, M.M. Gao, X.P. Liao, B. Shi, *Green Chem.* 13 (2011) 651–658.
- [62] H. Zhang, X. Li, G.J. Chen, *J. Mater. Chem.* 19 (2009) 8223–8231.
- [63] W. Xu, J.S. Kong, Y.-T.E. Yeh, P. Chen, *Nat. Mater.* 7 (2008) 992–996.